Front. Energy 2021, 15(3): 760–771
https://doi.org/10.1007/s11708-021-0781-9

RESEARCH ARTICLE

Ziwei ZHAO, Kaiyi CHEN, Jingwei HUANG, Lei WANG, Houde SHE, Qizhao WANG

Enhanced performance of $NiF_2/BiVO_4$ photoanode for photoelectrochemical water splitting

© Higher Education Press 2021

Abstract The serious surface charge recombination and fatigued photogenerated carriers transfer of the $BiVO_4$ photoanode restrict its photoelectrochemical (PEC) water splitting performance. In this work, nickel fluoride (NiF_2) is applied to revamp pure $BiVO_4$ photoanode by using a facile electrodeposition method. As a result, the as-prepared $NiF_2/BiVO_4$ photoanode increases the dramatic photocurrent density by approximately 180% compared with the pristine $BiVO_4$ photoanode. Furthermore, the correlative photon-to-current conversion efficiency, the charge injection, and the separation efficiency, as well as the hydrogen generation of the composite photoanode have been memorably enhanced due to the synergy of NiF_2 and $BiVO_4$. This study may furnish a dependable guidance in fabricating the fluoride-based compound/semiconductor composite photoanode system.

Keywords $BiVO_4$, NiF_2, heterojunction, photoelectrochemical water splitting

Received Mar. 12, 2021; accepted Jun. 20, 2021; online Sept. 15, 2021

Ziwei ZHAO, Jingwei HUANG, Lei WANG, Houde SHE
College of Chemistry and Chemical Engineering, Northwest Normal University, Lanzhou 730070, China

Kaiyi CHEN
School of Water and Environment, Key Laboratory of Subsurface Hydrology and Ecological Effects in Arid Region of the Ministry of Education, Chang'an University, Xi'an 710054, China

Qizhao WANG (✉)
College of Chemistry and Chemical Engineering, Northwest Normal University, Lanzhou 730070, China; School of Water and Environment, Key Laboratory of Subsurface Hydrology and Ecological Effects in Arid Region of the Ministry of Education, Chang'an University, Xi'an 710054, China
E-mails: wangqizhao@163.com; qzwang@chd.edu.cn

Special Issue: Photocatalysis: From Solar Light to Hydrogen Energy (Guest Editors: Wenfeng SHANGGUAN, Akihiko KUDO, Zhi JIANG, Yuichi YAMAGUCHI)

1 Introduction

Conversion of solar power into chemical energy by photoelectrochemical (PEC) water splitting is a promising and efficient strategy for accommodating the growth of miscellaneous energy utilization and environment protection requirements [1–5]. Up to the present, the metal oxide semiconductor, including TiO_2 [6,7], WO_3 [8,9], ZnO [10], and α-Fe_2O_3 [11–13], with an impressive photoelectrochemical activity have been developed and investigated.

Bismuth vanadate ($BiVO_4$) is regarded as an expectant photoanode owing to its narrow energy gap (approximately 2.4 eV), suitable band edge position, low cost, good chemical stability, and relatively high theoretical solar-to-hydrogen conversion efficiency [14–16]. However, the PEC capacities and application of $BiVO_4$ is mainly restricted by its short carrier diffusion length, poor electron-hole separation efficiency, and slow water oxidation kinetics [17,18]. To overcome these suppression factors, all kinds of strategies, such as morphological control [19–21], element doping [22,23], oxygen evolution catalysts layer loading [24,25] and heterojunction engineering [26–28], have been committed to improvement of PEC performance in water splitting.

According to Refs. [29,30], the layer of formation metal fluoride-based materials on $BiVO_4$ photoanodes significantly improves the PEC performance, which principally benefits from the following preponderance. Fluoride-based materials can adsorb ample visible light to provide sufficient energy for the separation between photogenerated electron-hole pairs due to the distinct optical properties [31]. Owing to the fact that fluorine anion has the strongest electronegativity, the metal-fluorine bond possesses the characteristics of strong iconicity and high polarization, bringing about the raised electron transfer efficiency [32]. Meanwhile, the metal-fluorine bond easily dissociates to form metal oxides (or hydroxide) as a passivation layer, which can maintain the stable catalyst structure and facilitate the photoanode water oxidation

reaction [33]. Additionally, the formation of heterojunctions between metal-fluoride and $BiVO_4$ can effectively increase the efficiency of the separation of electrons and holes [29]. Related research reports demonstrate that nickel fluoride (NiF_2) has relatively excellent performance in the field of electrocatalysis and batteries. Since there are related reports in the field of electrocatalysis and batteries that it has a relatively excellent performance, the research on nickel fluoride (NiF_2) has been continuously conducted [34,35]. Inspired by the results of electrochemical research, it may be a promising strategy to modify NiF_2 on the semiconductor photoanode to improve its PEC performance.

In this study, a novel hetero-structured photoanode was generated by electrodepositing NiF_2 onto the surface of $BiVO_4$ film. The as-prepared $NiF_2/BiVO_4$ photoanode demonstrates a dramatically improved PEC water oxidation property. Essentially, the outstanding PEC performance can be put down to the formed heterostructure between NiF_2 and $BiVO_4$, leading to the improved charge separation efficiency and the accelerative surface reaction kinetics. Furthermore, a feasible mechanism for explaining the increased phenomenon was reasonably speculated.

2 Experimental

2.1 Chemicals

KI, $C_4H_6O_2$, $VO(acac)_2$, DMSO, $Bi(NO_3)_2\cdot 5H_2O$, $Ni(NO_3)_2\cdot 6H_2O$, NaF, NaCl, NaOH, and C_2H_5OH were purchased from Sinopharm Chemical Reagent Co., Ltd. All the above raw materials were analytical reagent (AR) grade and used without further purification. Fluorine-doped tin oxide (FTO) coated glasses substrates were obtained from Zhuhai Kaivo Electronic Components Co., Ltd.

2.2 Method

The synthesis pathway of the samples is schematically illustrated in Fig. 1. $BiVO_4$ photoanodes were fabricated by electrodeposition and the annealing method [36]. Primarily, 20 mmol of KI was dissolved in 50 mL of deionized water, whose pH value was then adjusted to 1.6 by appending 1 mol/L HNO_3. Afterwards, 5 mmol of $Bi(NO_3)_3\cdot 5H_2O$ was added to the above mixed solution. Immediately, 20 mL of 0.23 mol/L p-benzoquinone ethanol solution was added to the above solution and stirred forcefully. A typical three-electrode system was used for electrodeposition which was conducted by cyclic voltammetry (CV) at a potential range of –0.13 to 0 V (versus Ag/AgCl), with a scan rate of 5 mV/s at room temperature. The obtained BiOI film was washed by deionized water and dried in an oven at 60°C. Subsequently, the 100 μL of 0.2 mol/L $VO(acac)_2$ DMSO solution was dropped onto the BiOI film and kept at 450°C for 2 h. To get rid of excess V_2O_5 on the surface of $BiVO_4$, the acquired film was immersed in 1 mol/L of NaOH solution for 30 min. Eventually, the as-prepared $BiVO_4$ electrode was adequately rinsed with deionized water and desiccated at air atmosphere.

The NiF_2 electrode and $NiF_2/BiVO_4$ electrode were electrodeposited by cyclic voltammetry in an electrochemical workstation with the three electrodes. The electrolyte was as follows: 5 mmol of $Ni(NO_3)_2\cdot 6H_2O$ was dissolved into 1 mol/L hydrogen peroxide solution. Then 5 mmol of NaF and 5 mmol of NaCl were added to the above solution and stirred for 30 min to form a homogeneous solution. The as-prepared $BiVO_4$ electrode was placed in a precursor solution. Afterwards, potentials were swept from –0.52 to 0.41 V (versus Ag/AgCl) at a scan rate of 0.1 V/s for 5 cycles, denoted as $NiF_2/BiVO_4$. Meanwhile, pure NiF_2 electrode was synthesized by the similar approach but scanned for 20 cycles.

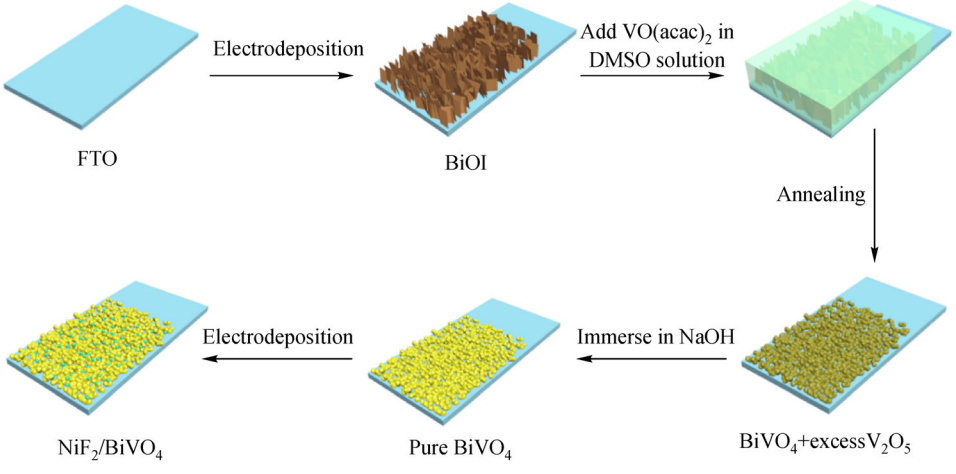

Fig. 1 Schematic illustration of the synthesis approach of $NiF_2/BiVO_4$ composite electrodes.

2.3 Characterization and PEC measurements

The X-ray diffraction (XRD) data patterns were measured on a Bragg-Brentano Rigaku D/MAX-2200/PCX-diffractometer with Cu Kα radiation (40 kV × 20 mA). The surface morphology of the electrodes was observed by using a JSM-6701F field emission scanning electron microscope (FE-SEM) and a JEOL JEM-2100 transmission electron microscopy (TEM). The X-ray photoelectron spectroscopy (XPS) was characterized by the PHI5702 photoelectron spectrometer. Using Ba_2SO_4 as the reflectance standard, the UV-vis diffuse reflectance spectra were observed by using a double-beam UV-vis spectrophotometer (UV-3100). The photoluminescence (PL) spectrum detection of samples was recorded on a PELS-55 luminescence/fluorescence spectrophotometer.

The PEC activity of photoanodes was evaluated on an electrochemical analyzer (CHI 760E) under a Xenon lamp illumination, which simulates sunlight resource AM 1.5 G (100 mW/cm^2). The electrolyte was 0.5 mol/L of Na_2SO_4 aqueous solution (pH = 7.35). All measurements were conducted on the condition of light irradiates to the back side of the FTO glass. All the used voltage values were converted to a reversible hydrogen electrode (RHE) through the formula ($E_{RHE} = E_{Ag/AgCl} + 0.197 + 0.059 \times pH$, of which 0.197 is the Ag/AgCl electrode with 3.5 mol/L KCl relative to the voltage value of the standard hydrogen electrode). The evolution of H_2 and O_2 gases were measured by using the GC-9560 gas chromatography.

3 Results and discussion

The crystalline phases of all the as-prepared electrodes were investigated by XRD analysis. As shown in Fig. 2(a), the clear diffraction peaks stemmed from $BiVO_4$ can be well indexed to a monoclinic scheelite crystal system (JCPDS. No. 14-0688) [37]. Apart from the peaks of SnO_2 ingredient of FTO substrates (JCPDS No. 46-1088), no impurity diffraction peaks can be observed. However, in the pattern of $NiF_2/BiVO_4$, the characteristic diffraction peaks of NiF_2 nanoparticles cannot be distinctly observed (JCPDS No. 22-0749), which might be attributed to the diffraction peaks of NiF_2 overlap with that of $BiVO_4$ [38]. Yet, despite these, the TEM image of the $NiF_2/BiVO_4$ electrode indicates that a layer of fine NiF_2 nanoparticles was loaded on the $BiVO_4$ film, as presented in Figs. 2(b) and 2(c). More specifically, the high-crystalline structure

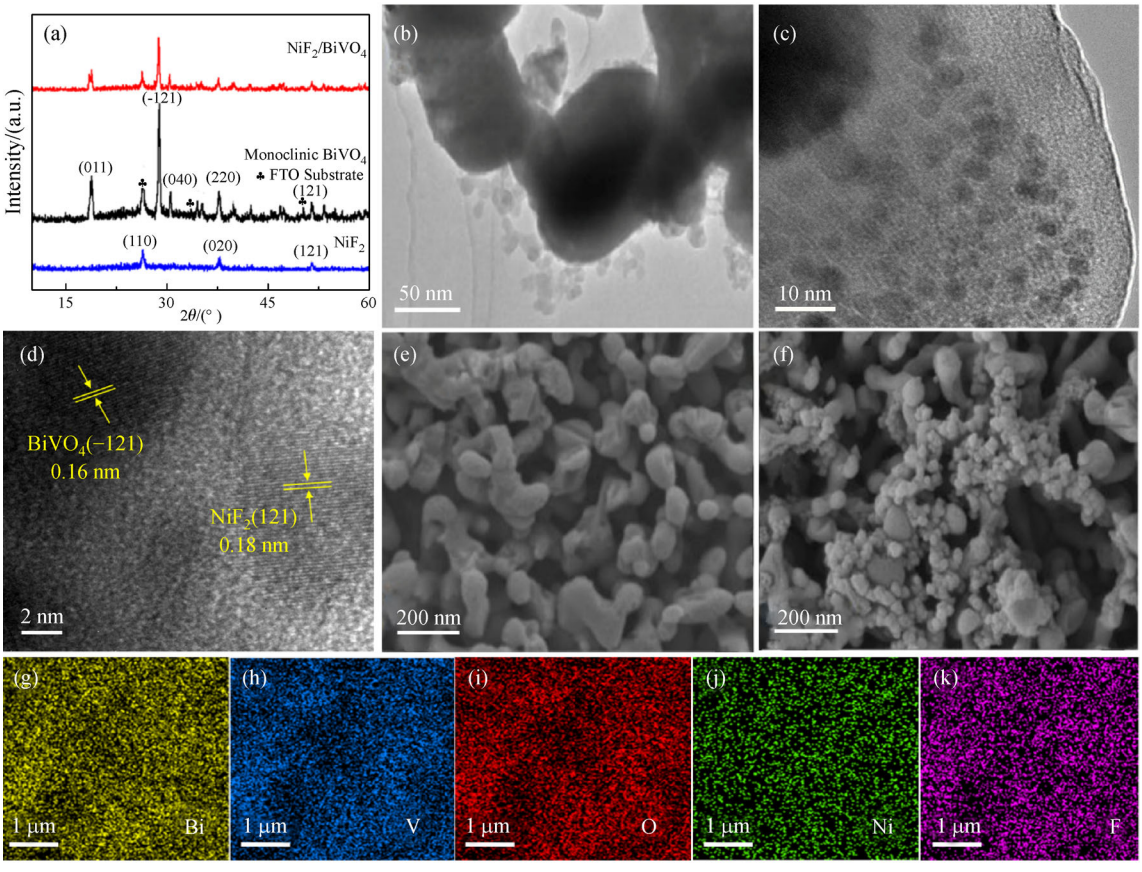

Fig. 2 Structure and morphology characterization.
(a) XRD patterns of $BiVO_4$, NiF_2, $NiF_2/BiVO_4$ electrodes; (b–d) TEM and HR-TEM images of $NiF_2/BiVO_4$ composite sample; (e) SEM images of $BiVO_4$; (f) SEM images of $NiF_2/BiVO_4$ electrodes; (g–k) SEM-EDS elemental mapping images of Bi, V, O, Ni, and F respectively.

with a lattice spacing of 0.16 nm and 0.18 nm corresponding to the (–121) plane of $BiVO_4$ and the (121) plane of NiF_2 respectively could be visibly observed in Fig. 2(d) [30]. In the meantime, it can be clearly seen that there is an obvious interface between $BiVO_4$ and NiF_2. These results attest that $NiF_2/BiVO_4$ has been successfully prepared. The surface morphology and microstructure of all the photoanodes are reflected by FE-SEM. From Fig. 2(e), it can be observed that a pure $BiVO_4$ with a wormlike structure and a smooth surface is coated on the surface of the FTO conductive glass. After electrodeposition, the NiF_2 nanoparticles are uniformly dispersed on the surface of $BiVO_4$, as demonstrated in Fig. 2(f). Additionally, it can be realized from the related element mappings of the $NiF_2/BiVO_4$ (Figs. 2(g)–2(k)) that the Bi, V, O, Ni, and F elements are scattered evenly in the composite electrode, which also indicates the successful preparation of the photoanode material.

The chemical bonding state of the $NiF_2/BiVO_4$ photoanode was inquired by XPS, as exhibited in Fig. 3. The full spectrum of the composite photoanode is presented in Fig. 3(a). It can be precisely observed that the as-prepared sample is composed of Bi, V, O, Ni, and F elements, in accordance with the elemental mapping consequence. Figure 3(b) displays two different peaks located at 159.0 eV and 164.3 eV, which can be attributed to the Bi $4f_{7/2}$ and Bi $4f_{5/2}$, respectively [39]. Simultaneously, Fig. 3(c) demonstrates that the V $2p_{3/2}$ and V $2p_{1/2}$ orbital peaks are situated at 516.3 eV and 523.8 eV respectively. As depicted in Fig. 3(d), two peaks can be clearly identified in the O1s core level spectra. In detail, the peak at 531.0 eV is in accordance with the lattice oxygen while the peak at 532.7 eV can be ascribed to O 1s that is associated with hydroxy species of surface-adsorbed water molecules [40]. The characteristic peaks of Ni element were investigated, as manifested in Fig. 3(e). The two broad peaks at 861.3 and 878.9 eV are identified as shake-up satellites (marked as "Sat.") of Ni $2p_{3/2}$ and Ni $2p_{1/2}$. Synchronously, the two peaks at 855.1 eV and 872.7 eV can be ascribed to Ni $2p_{3/2}$ and Ni $2p_{1/2}$ respectively, which is a convincible justification to the existence of the oxidation state of Ni^{2+} [41]. Figure 3(f) reveals that the peaks of F 1s core-levels are located at 684.2 eV, indicating a normal state of F^- in the electrode sample [30]. This further illustrates that the NiF_2 has been successfully loaded on the surface of the pristine $BiVO_4$.

Moreover, in order to assess the optical properties, the UV-vis diffuse reflectance spectra of the NiF_2, $BiVO_4$ and $NiF_2/BiVO_4$ electrodes were presented Fig. 4(a). It can be demonstrated that the absorption edge of NiF_2 and $BiVO_4$ are at the wavelength of 530 and 510 nm, respectively. Remarkably, the absorption intensity of $BiVO_4$ to light is

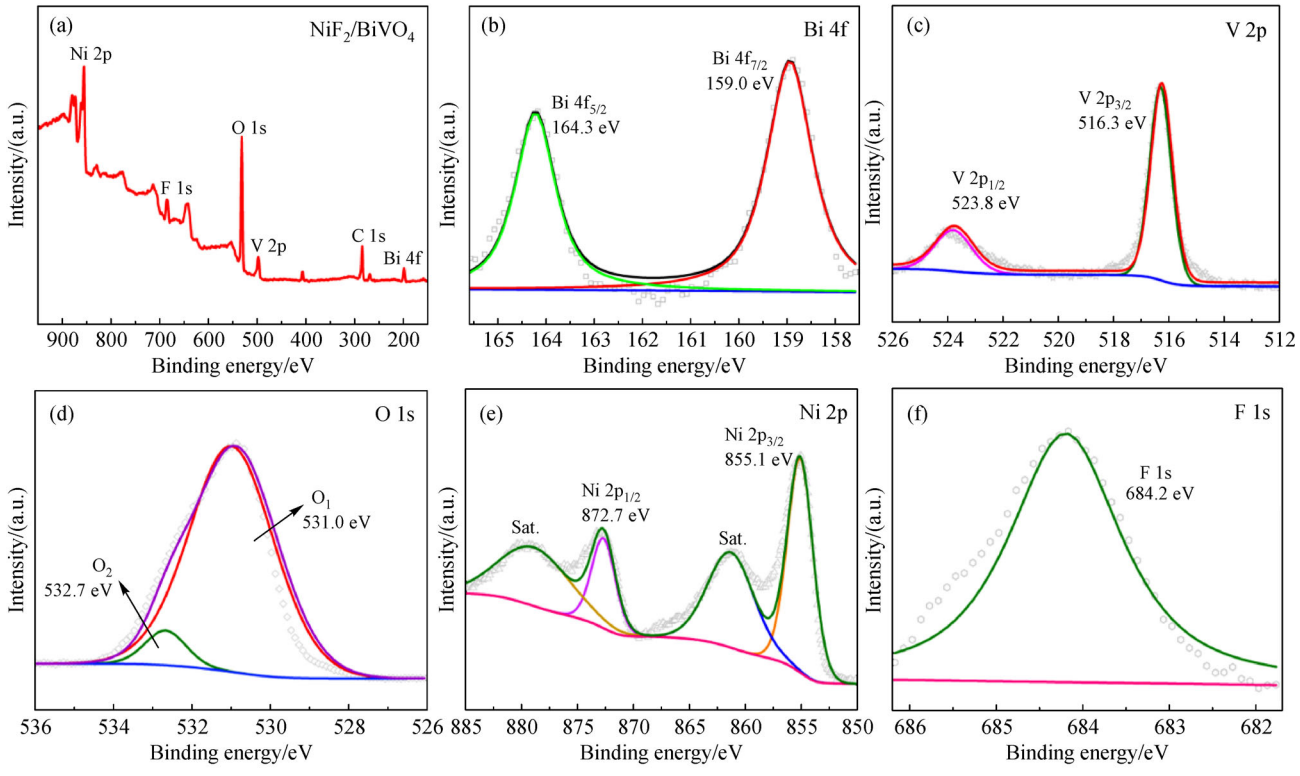

Fig. 3 XPS spectra.

(a) Wide survey XPS spectrum; (b) Bi 4f XPS spectra of the $NiF_2/BiVO_4$ electrode; (c) V 2p XPS spectra of the $NiF_2/BiVO_4$ electrode; (d) O 1s XPS spectra of the $NiF_2/BiVO_4$ electrode; (e) Ni 2p XPS spectra of the $NiF_2/BiVO_4$ electrode; (f) F 1s XPS spectra of the $NiF_2/BiVO_4$ electrode.

enhanced after the deposition of NiF_2 nanoparticles. In the meantime, the absorption edge of $NiF_2/BiVO_4$ is located at approximately 525 nm, which indicates an obvious red-shift compared to the $BiVO_4$ photoanode. Meanwhile, the band gap of all the photoanodes could be calculated by the Tauc equation (Fig. 4(b)). According to Tauc relationship, the energies of the band gap are 2.46, 2.49, and 2.48 eV for the NiF_2, $BiVO_4$ and $NiF_2/BiVO_4$ electrodes, respectively. The slight decrease of enery gap (Eg) reflected the broadening of absorption spectrum range, which is beneficial to the enhancement of absorption capability [42]. The photoluminescence (PL) spectra technology is applied to effectively analyze the separation and recombination performance of photo-induced carriers [43]. It can be found in Fig. 4(c) that the peak intensity of the $NiF_2/BiVO_4$ electrode was weaker than that of the pristine $BiVO_4$ electrode, which indicates the tardy recombination rate of photogenerated electron-holes and the elevated charge separation efficiency.

The photoelectrochemical activities of as-prepared photoanodes for water splitting were appraised in 0.5 mol/L Na_2SO_4 under simulated solar light irradiation (AM 1.5 G). The linear sweep voltammetry (LSV) curves explicitly disclose that the photocurrent density of the pristine $BiVO_4$ is 1.0 mA/cm^2 at 1.23 V_{RHE}, as presented in Fig. 5(a). It is worth mentioning that the photocurrent density of the $NiF_2/BiVO_4$ composite photoanode is up to 2.8 mA/cm^2 at 1.23 V_{RHE}, which is 2.8 times that of $BiVO_4$ photoanode. Furthermore, the $NiF_2/BiVO_4$ electrode demonstrates a much lower onset potential and a steeper curve in comparison to the $BiVO_4$ electrode in Fig. 5(b). In detail, the onset potential of $NiF_2/BiVO_4$ electrode exhibits a negative shift of approximately 210 mV compared with the pure $BiVO_4$ electrode under dark condition. At the same time, the NiF_2 electrode possesses the highest current density and exhibits a favorable electrocatalytic performance, which improves the performance of the $NiF_2/BiVO_4$ electrode. These results reveal that the $BiVO_4$ electrode modified with NiF_2 demonstrates a better water oxidation ability.

To further expound the separation course of photogenerated electrons and holes in detail, the electrochemical impedance spectroscopy (EIS) measurements of the bare $BiVO_4$ and $NiF_2/BiVO_4$ photoanodes with light illumination were conducted, as depicted in Fig. 5(c). Apparently, through the exhibition of the radius of the Nyquist

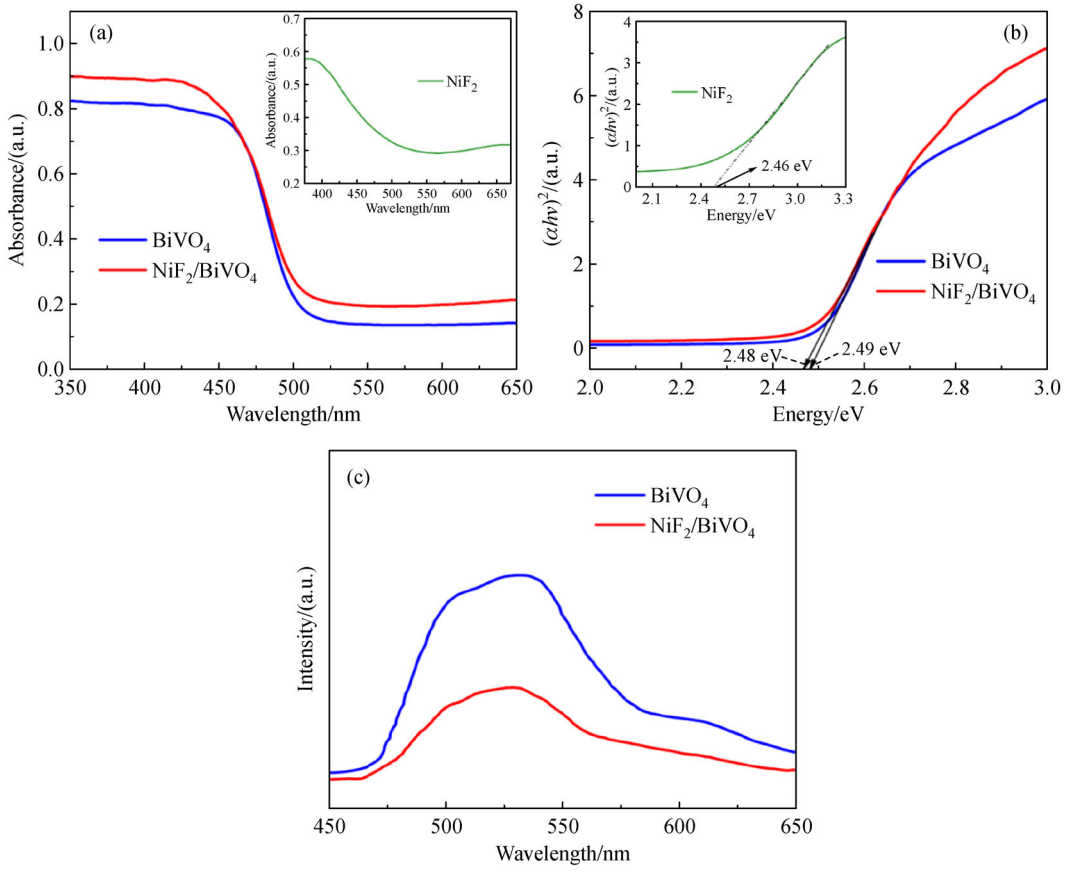

Fig. 4 Characterization of optical properties.

(a) UV-vis diffused reflectance spectra; (b) band gap energy of the $BiVO_4$ and $NiF_2/BiVO_4$ photoanodes; (c) PL emission spectra of the as-prepared electrodes.

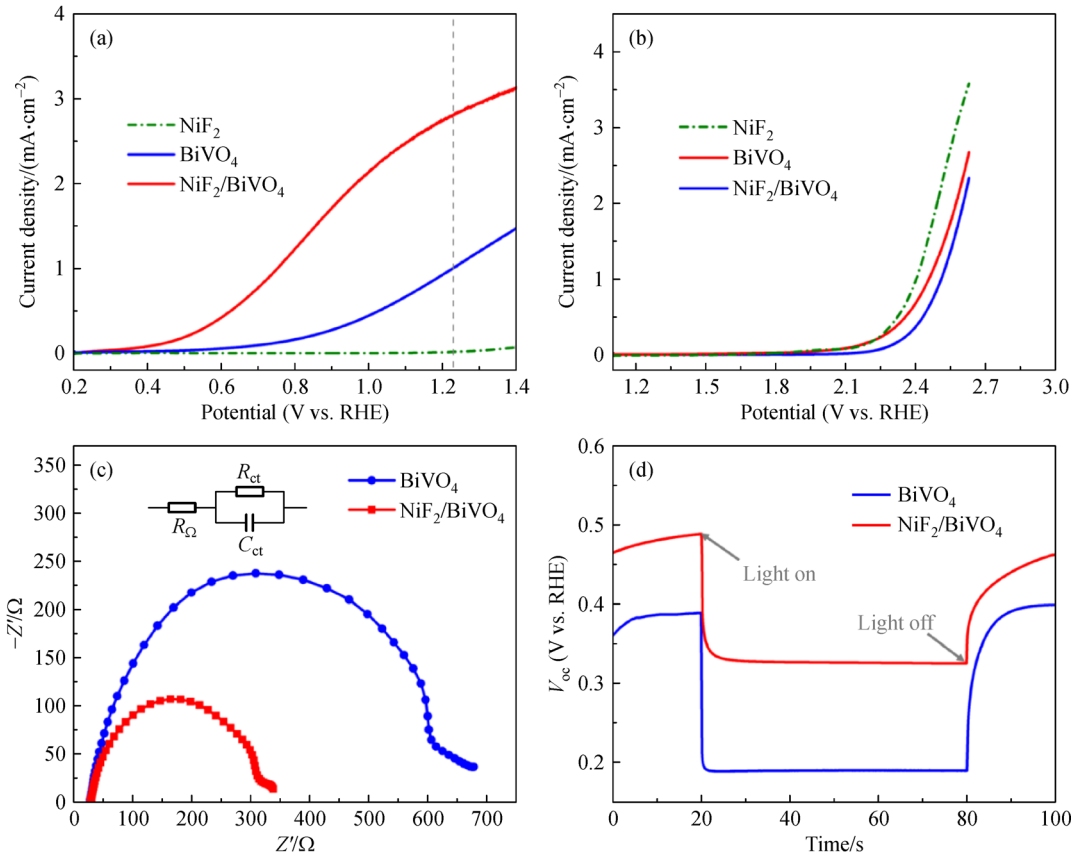

Fig. 5 LSV curves of NiF_2, $BiVO_4$, and $NiF_2/BiVO_4$ photoanodes.
(a) Under illumination; (b) without illumination; (c) EIS results acquired at 1.23 V_{RHE} ; (d) V_{oc} versus time curves investigated in the 0.5 mol/L Na_2SO_4 solution.

diagram, a smaller arc radius appears for $NiF_2/BiVO_4$ in light irradiation condition compared with $BiVO_4$. Consequently, the relevant Randle equivalent circuit model can be obtained (the correlative Randle circuit values being presented in Table 1), where R_Ω represents the resistance corresponding to the charge transfer (including the resistance of the catalyst, the FTO substrate, the electrolyte, and the wire connection in the circuit), and the R_{ct} and C_{ct} respectively represent the resistance and capacitance related to charge transfer on the electrode/electrolyte interface [30,44,45]. This impedance decrement can be mainly put down to the swifter transference of photogenerated holes on the surface of $NiF_2/BiVO_4$ electrode.

Simultaneously, to explore the possible cause for the result in the different PEC performance of the bare $BiVO_4$ and $NiF_2/BiVO_4$ photoanodes, the transfer kinetics of these electrodes were illustrated by the variation of open-circuit voltage (V_{oc}) [46]. The open-circuit voltage decay rate is a significant criterion of applying to understand the situation of the electron recombination [47]. As shown in Fig. 5(d), the V_{oc} curve of the $NiF_2/BiVO_4$ photoanode demonstrates a slower decay rate than that of the $BiVO_4$ photoanode under the identical condition, which reveals that the recombination of the photogenerated carriers are efficiently suppressed.

Table 1 Fitted results of EIS data using Randle equivalent circuit

Sample	R_Ω/Ω (*Error*/%)	R_{ct}/Ω (*Error*/%)	C_{ct}/F (*Error*/%)
$BiVO_4$	27.8 (0.37)	622.6 (0.43)	5.236e–5 (1.50)
$NiF_2/BiVO_4$	28.5 (0.38)	298.2 (0.45)	8.082e–5 (2.01)

Moreover, the applied bias photo-to-current efficiency (ABPE) value of the $NiF_2/BiVO_4$ composite photoanode reaches up to 0.56% at 0.88 V_{RHE}, while the pristine $BiVO_4$ photoanode only achieves an efficiency of 0.1% at 1.0 V_{RHE}, which is consistent with the value of their photocurrent density (Fig. 6(a)). Based on the performances above, it can be concluded that the surface modification of NiF_2 could efficaciously improve the PEC water oxidation activity and inhibit the recombination of the photogenerated electron-hole pairs of the pristine $BiVO_4$ photoanode. The photoanode competence can be evaluated by the incident photo-to-current conversion efficiency (IPCE) [48]. When the light wavelength ranges from 360 to 520 nm, the IPCE magnitudes of $NiF_2/BiVO_4$ photoanode is higher than that of the pure $BiVO_4$ photoanode (Fig. 6(b)). To be specific, the $NiF_2/BiVO_4$

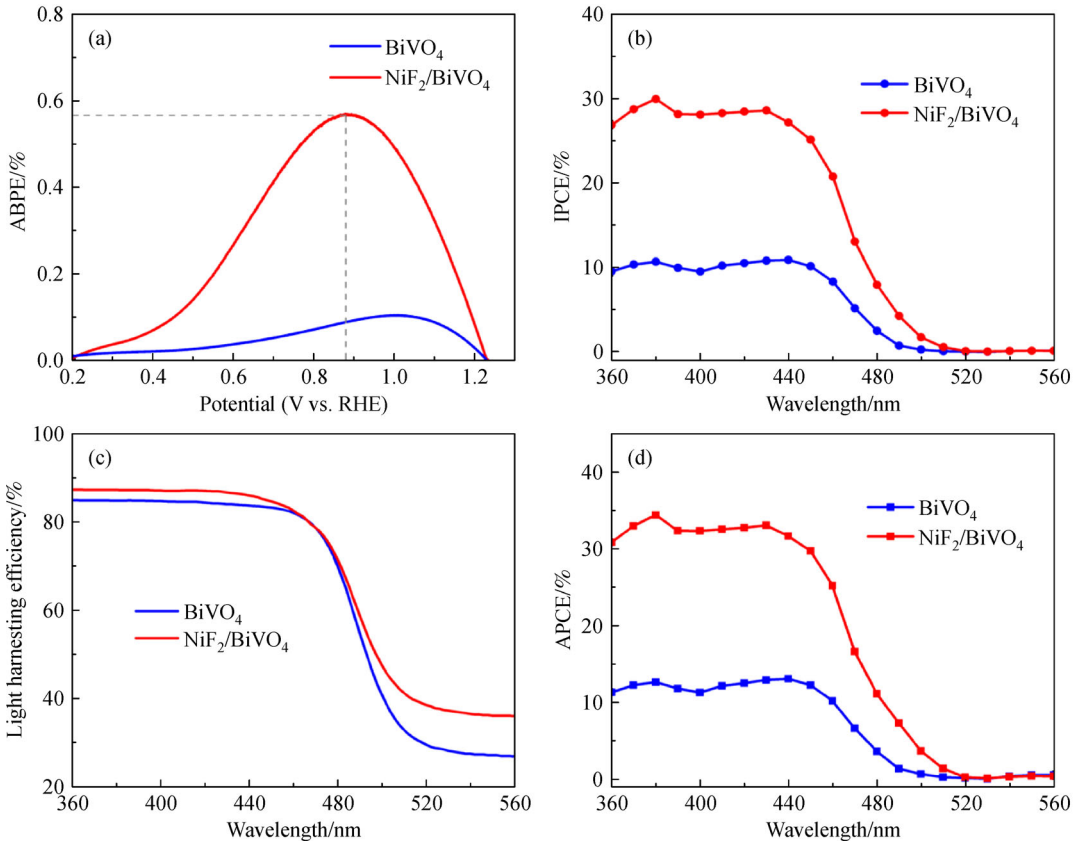

Fig. 6 Photoelectric conversion efficiency.

(a) ABPE of the $BiVO_4$ and $NiF_2/BiVO_4$ photoanodes; (b) IPCE of the $BiVO_4$ and $NiF_2/BiVO_4$ photoanodes; (c) LHE of the $BiVO_4$ and $NiF_2/BiVO_4$ photoanodes; (d) APCE of the $BiVO_4$ and $NiF_2/BiVO_4$ photoanodes.

photoanode achieves a maximum IPCE value of 30% at 380 nm, which is 3 times higher than that of the pure $BiVO_4$ photoanode at the alike wavelength. Meanwhile, the promotion of the light harvesting efficiency (LHE) of the composite photoanode will give rise to the increase of the photo-to-electron efficiency (Fig. 6(c)). Consequently, the absorbed photo-to-current conversion efficiency (APCE) of the $NiF_2/BiVO_4$ photoanode is computed as 34% at 380 nm, while the pristine $BiVO_4$ photoanode can only reach 13% at the identical wavelength, as shown in Fig. 6(d). Sequentially, it can be concluded that the $NiF_2/BiVO_4$ photoanode may make use of the absorbed light more effectively.

As displayed in Fig. 7(a) and 7(b), by integrating IPCE on the AM 1.5 G solar spectrum, the photocurrent densities of $BiVO_4$ and $NiF_2/BiVO_4$ are calculated as 0.69 mA/cm^2 and 2.35 mA/cm^2, respectively. These estimated values are very close to the actual measured values in the LSV curve, indicating that all measurement procedures are trustworthy [49].

Whether the measured photoanode has a significant PEC performance can be reflected by the proportion of holes participating in the entire water splitting reaction. At the same time, the proportion of holes which participates in the PEC reaction are estimated by the charge injection efficiency, which is obtained by dividing the photocurrent density for the water oxidation by the photocurrent density for the Na_2SO_3 oxidation under identical circumstances [50,51]. As presented in Fig. 8(a), the charge injection efficiency of the pure $BiVO_4$ photoanode is maintained 19% at 1.23 V_{RHE}, implying that a large proportion of the generated holes are unutilized because of the bulk recombination. In contrast, after modifying with NiF_2 on the surface of $BiVO_4$, the charge injection efficiency of the composite photoanode is attained to 48% at 1.23 V_{RHE}, which is 2.5 times higher than that of the pristine $BiVO_4$ photoanode. In the meantime, the charge separation efficiency also appears to be an analogous situation as the charge injection efficiency, as demonstrated in Fig. 8(b). It further confirms the promoted separation of photogenerated electrons and holes after bringing in NiF_2.

Hydrogen and oxygen can be acquired through the participation of $NiF_2/BiVO_4$ electrode in the photoelectrochemical water splitting process. As shown in Fig. 9(a), after three hours of photoelectric reaction, the generated magnitudes of H_2 to O_2 conform to the molar ratio of approximately 2:1. Synchronously, the calculated average Faradaic efficiencies of H_2 and O_2 reactions are both

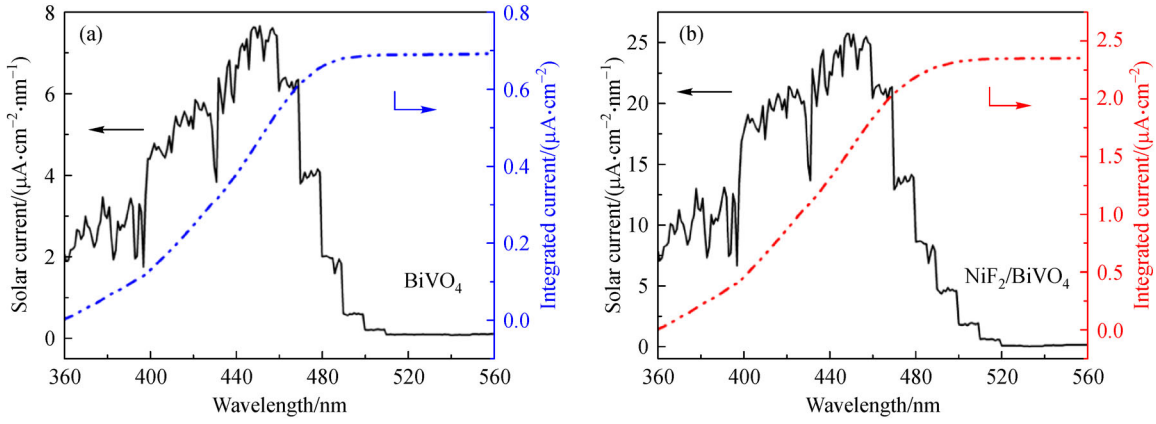

Fig. 7 Solar currents.
(a) $BiVO_4$; (b) $NiF_2/BiVO_4$ electrode samples (left ordinate) and the integrated photocurrents at 1.23 V_{RHE} (right ordinate).

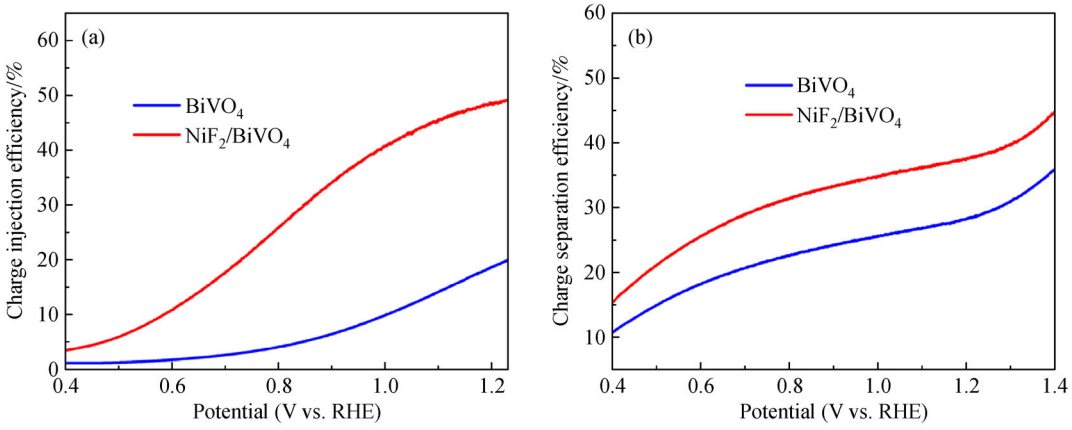

Fig. 8 Charge injection and separation efficiency.
(a) Charge injection efficiency; (b) charge separation efficiency of bare $BiVO_4$ and $NiF_2/BiVO_4$ photoanodes.

Table 2 PEC measurement results of $BiVO_4$ and $NiF_2/BiVO_4$ photoanodes

Sample	$BiVO_4$	$NiF_2/BiVO_4$
Current density(mA/cm^2 at 1.23 V_{RHE})	1.0	2.8
Onset potential (V_{RHE})	2.14	1.93
ABPE/%	0.1	0.56
IPCE/%	11	30
APCE/%	13	34
Charge injection efficiency/%	19	48
Charge separation efficiency/%	27	36

approximately 90%. As a result, it sufficiently elucidates that the photogenerated charges are almost completely used for decomposing water to obtain hydrogen and oxygen. Stability is an important indicator to evaluate the catalytic performance and the application value of the photoanode. As presented in Fig. 9(b), the $NiF_2/BiVO_4$ photoanode can maintain 83% of the initial photocurrent density under 3 h of constant light illumination, indicating that it has a relatively favorable stability.

As a consequence, based on the above characterization and properties, a possible mechanism of the NiF_2 effectively which improved the PEC water splitting performance of the $BiVO_4$ photoanode was proposed. Initially, based on the correlative energy gap and Mott-Schottky curves of the NiF_2 and $BiVO_4$ (Figs. 9(c) and 9(d)), it can be concluded that both of the semiconductors exhibit the *n*-type behavior. Based on Fig. 10, it can be comprehended that the positions of the conduction band (CB) and the valence band (VB) of $BiVO_4$ and NiF_2 are (0.21, 2.70 eV) and (–0.12, 2.34 eV), respectively [52]. These results demonstrate that they possess more appropriate band matching, which promotes a more efficient separation of the photogenerated electrons and holes [53,54]. Specifically speaking, benefited from the *n-n* heterostructure formed between the NiF_2 and $BiVO_4$, the photogenerated electrons in the CB of NiF_2 migrate to the

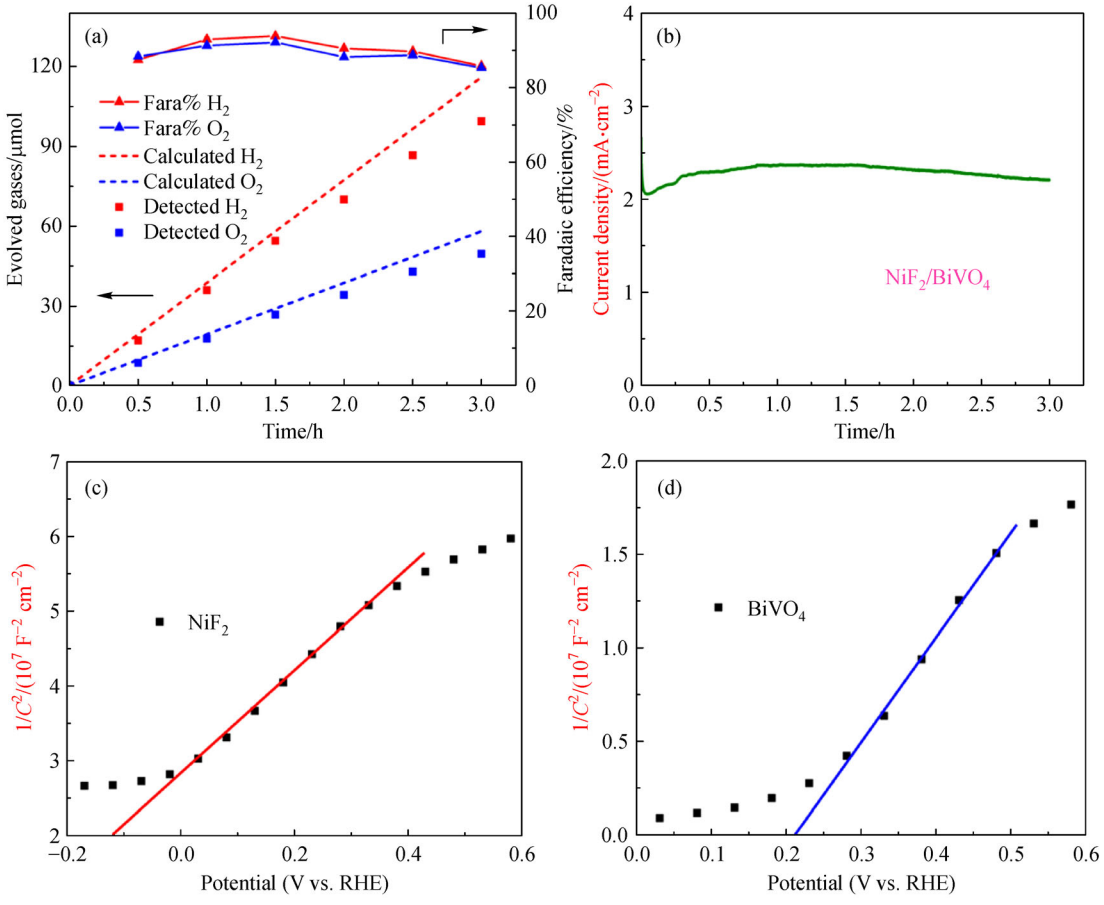

Fig. 9 Effect of H_2 and O_2 production, stability of the photoanode, and Mott-Schottky curves.
(a) H_2 and O_2 gases evolution of the $NiF_2/BiVO_4$ photoanode compared with the evolution expected from the current acquisition; (b) stability curve of the $NiF_2/BiVO_4$ photoanode under 3 h of light illumination; (c) Mott-Schottky plots of NiF_2 obtained in the dark condition; (d) Mott-Schottky plots of $BiVO_4$ acquired in the dark condition (C is the interfacial capacitance.).

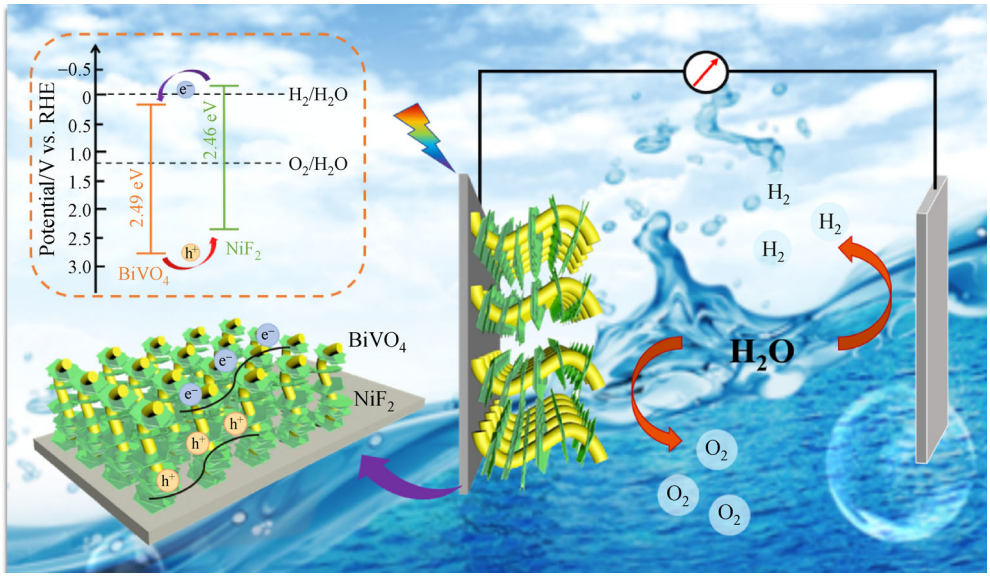

Fig. 10 Possible mechanism schematic depiction of $NiF_2/BiVO_4$ photoelectrode for PEC water splitting application.

CB of $BiVO_4$. These electrons will eventually be transferred to the Pt counter electrode for the reduction of H^+ into H_2. Meanwhile, the photogenerated holes at the VB of $BiVO_4$ migrate to the CB of NiF_2 and further oxidize water molecules to acquire O_2 [30,55–57]. Consequently, the heterostructure $NiF_2/BiVO_4$ composite photoanode can efficiently inhibit the charge recombination and enhance the PEC performance. Furthermore, NiF_2 as an electrocatalyst, not only can efficaciously decrease the overpotential, but also can suitably accelerate the surface reaction kinetics and facilitate the electrons and holes separation [40,58].

4 Conclusions

This paper demonstrated a facile electrodeposition approach to fabricate the $NiF_2/BiVO_4$ heterojunction photoanode for photoelectrochemical water splitting. The $NiF_2/BiVO_4$ composite photoanode was found to display a higher photocurrent density of 2.8 mA/cm^2 at 1.23 V_{RHE} under AM 1.5 G illumination, which was 2.8 times than that of the pristine $BiVO_4$ photoanode. In addition, further systematized exploration revealed that the photogenerated electrons-holes separation and surface reaction kinetics were effectually improved when NiF_2 was assembled onto the surface of the $BiVO_4$ photoanode. Consequently, this research thoroughly explored the impact of metal fluoride on the PEC ability of $BiVO_4$ photoanode, providing a profound insight into the construction of a high-performance heterojunction photoanode system.

Acknowledgements This work was financially supported by the National Key Research and Development Program of China (Grant No. 2017YFC0602306), the National Natural Science Foundation of China (Grant No. 21808189), and National Natural Science Foundation of Gansu Province (Grant No. 20JR5RA523).

References

1. Ye S, Ding C, Chen R, et al. Mimicking the key functions of photosystem II in artificial photosynthesis for photoelectrocatalytic water splitting. Journal of the American Chemical Society, 2018, 140(9): 3250–3256
2. He W, Wang R, Zhang L, et al. Enhanced photoelectrochemical water oxidation on a $BiVO_4$ photoanode modified with multifunctional layered double hydroxide nanowalls. Journal of Materials Chemistry A, Materials for Energy and Sustainability, 2015, 3(35): 17977–17982
3. Han H S, Shin S, Kim D H, et al. Boosting the solar water oxidation performance of a $BiVO_4$ photoanode by crystallographic orientation control. Energy & Environmental Science, 2018, 11(5): 1299–1306
4. Cao X, Xu C, Liang X, et al. Rationally designed/assembled hybrid $BiVO_4$-based photoanode for enhanced photoelectrochemical performance. Applied Catalysis B: Environmental, 2020, 260: 118136
5. Tang Y, Wang R, Yang Y, et al. Highly enhanced photoelectrochemical water oxidation efficiency based on triadic quantum dot/layered double hydroxide/$BiVO_4$ photoanodes. ACS Applied Materials & Interfaces, 2016, 8(30): 19446–19455
6. Chen X, Xiong J, Shi J, et al. Roles of various Ni species on TiO_2 in enhancing photocatalytic H_2 evolution. Frontiers in Energy, 2019, 13(4): 684–690
7. Li C, Chen F, Ye L, et al. Preparation and photocatalytic hydrogen production of B, N co-doped In_2O_3/TiO_2. Acta Chimica Sinica, 2020, 78(12): 1448
8. Jun J, Ju S, Moon S, et al. The optimization of surface morphology of Au nanoparticles on WO_3 nanoflakes for plasmonic photoanode. Nanotechnology, 2020, 31(20): 204003
9. Ali H, Ismail N, Amin M S, Mekewi M. Decoration of vertically aligned TiO_2 nanotube arrays with WO_3 particles for hydrogen fuel production. Frontiers in Energy, 2018, 12(2): 249–258
10. Wan X, Wang L, Dong C L, et al. Activating kläui-type organometallic precursors at metal oxide surfaces for enhanced solar water oxidation. ACS Energy Letters, 2018, 3(7): 1613–1619
11. Kong T, Huang J, Jia X, et al. Nitrogen-doped carbon nanolayer coated hematite nanorods for efficient photoelectrocatalytic water oxidation. Applied Catalysis B: Environmental, 2020, 275: 119113
12. Masoumi Z, Tayebi M, Lee B K. The role of doping molybdenum (Mo) and back-front side illumination in enhancing the charge separation of α-Fe_2O_3 nanorod photoanode for solar water splitting. Solar Energy, 2020, 205: 126–134
13. Jiao T, Lu C, Zhang D, et al. Bi-functional Fe_2ZrO_5 modified hematite photoanode for efficient solar water splitting. Applied Catalysis B: Environmental, 2020, 269: 118768
14. Wang S, He T, Chen P, et al. *In situ* formation of oxygen vacancies achieving near-complete charge separation in planar $BiVO_4$ photoanodes. Advanced Materials, 2020, 32(26): 2001385
15. Ning X, Lu B, Zhang Z, et al. An efficient strategy for boosting photogenerated charge separation by using porphyrins as interfacial charge mediators. Angewandte Chemie International Edition, 2019, 58(47): 16800–16805
16. Zeng C, Hu Y, Zhang T, et al. A core–satellite structured Z-scheme catalyst $Cd_{0.5}Zn_{0.5}S/BiVO_4$ for highly efficient and stable photocatalytic water splitting. Journal of Materials Chemistry A, Materials for Energy and Sustainability, 2018, 6(35): 16932–16942
17. Meng Q, Zhang B, Fan L, et al. Efficient $BiVO_4$ photoanodes by postsynthetic treatment: remarkable improvements in photoelectrochemical performance from facile borate modification. Angewandte Chemie International Edition, 2019, 58(52): 19027–19033
18. Wang L, Zhang T, Su J, et al. Room-temperature photodeposition of conformal transition metal based cocatalysts on $BiVO_4$ for enhanced photoelectrochemical water splitting. Nano Research, 2020, 13(1): 231–237
19. Meng F, Zhang Q, Liu K, et al. Integrated bismuth oxide ultrathin nanosheets/carbon foam electrode for highly selective and energy-efficient electrocatalytic conversion of CO_2 to HCOOH. Chemistry (Weinheim an der Bergstrasse, Germany), 2020, 26(18): 4013–4018

20. Li Y, Zhang L, Xiang X, et al. Engineering of ZnCo-layered double hydroxide nanowalls toward high-efficiency electrochemical water oxidation. Journal of Materials Chemistry A, Materials for Energy and Sustainability, 2014, 2(33): 13250
21. Monny S A, Wang Z, Lin T, et al. Designing efficient $Bi_2Fe_4O_9$ photoanodes via bulk and surface defect engineering. Chemical Communications, 2020, 56(65): 9376–9379
22. Wang S, Zhang X. N-doped C@$Zn_3B_2O_6$ as a low cost and environmentally friendly anode material for Na-ion batteries: high performance and new reaction mechanism. Advanced Materials, 2019, 31(5): 1805432
23. Zhong H, Zhang Q, Wang J, et al. Engineering ultrathin C_3N_4 quantum dots on graphene as a metal-free water reduction electrocatalyst. ACS Catalysis, 2018, 8(5): 3965–3970
24. Xu C, Sun W, Dong Y, et al. A graphene oxide–molecular Cu porphyrin-integrated $BiVO_4$ photoanode for improved photoelectrochemical water oxidation performance. Journal of Materials Chemistry A, Materials for Energy and Sustainability, 2020, 8(7): 4062–4072
25. Zhang B, Wang L, Zhang Y, et al. Ultrathin FeOOH nanolayers with abundant oxygen vacancies on $BiVO_4$ photoanodes for efficient water oxidation. Angewandte Chemie, 2018, 130(8): 2270–2274
26. Luo L, Wang Z, Xiang X, et al. Selective activation of benzyl alcohol coupled with photoelectrochemical water oxidation via a radical relay strategy. ACS Catalysis, 2020, 10(9): 4906–4913
27. Gao B, Wang T, Fan X, et al. Selective deposition of Ag_3PO_4 on specific facet of $BiVO_4$ nanoplate for enhanced photoelectrochemical performance. Solar RRL, 2018, 2(9): 1800102
28. Wei D, Tan Y, Wang Y, et al. Function-switchable metal/semiconductor junction enables efficient photocatalytic overall water splitting with selective water oxidation products. Science Bulletin, 2020, 65(16): 1389–1395
29. Zhang B, Chou L, Bi Y. Tuning surface electronegativity of $BiVO_4$ photoanodes toward high-performance water splitting. Applied Catalysis B: Environmental, 2020, 262: 118267
30. Wang Q, Niu T, Wang L, et al. FeF_2/$BiVO_4$ heterojuction photoelectrodes and evaluation of its photoelectrochemical performance for water splitting. Chemical Engineering Journal, 2018, 337: 506–514
31. Chen P, Zhou T, Wang S, et al. Dynamic migration of surface fluorine anions on cobalt-based materials to achieve enhanced oxygen evolution catalysis. Angewandte Chemie International Edition, 2018, 57(47): 15471–15475
32. Meng F, Zhang Q, Duan Y, et al. Structural optimization of metal oxyhalide for CO_2 reduction with high selectivity and current density. Chinese Journal of Chemistry, 2020, 38(12): 1752–1756
33. Zhang D, Han X, Kong X, et al. The principle of introducing halogen ions into β-FeOOH: controlling electronic structure and electrochemical performance. Nano-Micro Letters, 2020, 12(1): 107
34. Liu H, Liu Z, Feng L. Bonding state synergy of the NiF_2/Ni_2P hybrid with the co-existence of covalent and ionic bonds and the application of this hybrid as a robust catalyst for the energy-relevant electrooxidation of water and urea. Nanoscale, 2019, 11(34): 16017–16025
35. Yang Z, Chang Z, Xu J, et al. CeO_2@$NiCo_2O_4$ nanowire arrays on carbon textiles as high performance cathode for Li-O_2 batteries. Science China, Chemistry, 2017, 60(12): 1540–1545
36. Zhou S, Yue P, Huang J, et al. High-performance photoelectrochemical water splitting of $BiVO_4$@Co-MIm prepared by a facile *in situ* deposition method. Chemical Engineering Journal, 2019, 371: 885–892
37. She H, Jiang M, Yue P, et al. Metal (Ni^{2+}/Co^{2+}) sulfides modified $BiVO_4$ for effective improvement in photoelectrochemical water splitting. Journal of Colloid and Interface Science, 2019, 549: 80–88
38. Zhou S, Chen K, Huang J, et al. Preparation of heterometallic CoNi-MOFs-modified $BiVO_4$: a steady photoanode for improved performance in photoelectrochemical water splitting. Applied Catalysis B: Environmental, 2020, 266: 118513
39. She H, Yue P, Ma X, et al. Fabrication of $BiVO_4$ photoanode cocatalyzed with NiCo-layered double hydroxide for enhanced photoactivity of water oxidation. Applied Catalysis B: Environmental, 2020, 263: 118280
40. She H, Yue P, Huang J, et al. One-step hydrothermal deposition of F: FeOOH onto $BiVO_4$ photoanode for enhanced water oxidation. Chemical Engineering Journal, 2020, 392: 123703
41. Deng J, Lv X, Zhang H, et al. Loading the FeNiOOH cocatalyst on Pt-modified hematite nanostructures for efficient solar water oxidation. Physical Chemistry Chemical Physics, 2016, 18(15): 10453–10458
42. Wang X, Zhou C, Shi R, et al. Two-dimensional $Sn_2Ta_2O_7$ nanosheets as efficient visible light-driven photocatalysts for hydrogen evolution. Rare Metals, 2019, 38(5): 397–403
43. Lu W, Zhang Y, Zhang J, et al. Reduction of gas CO_2 to CO with high selectivity by Ag nanocube-based membrane cathodes in a photoelectrochemical system. Industrial & Engineering Chemistry Research, 2020, 59(13): 5536–5545
44. She H, Zhao Z, Bai W, et al. Enhanced performance of photocatalytic CO_2 reduction via synergistic effect between chitosan and Cu: TiO_2. Materials Research Bulletin, 2020, 124: 110758
45. Yu Q, Meng X, Wang T, et al. Hematite films decorated with nanostructured ferric oxyhydroxide as photoanodes for efficient and stable photoelectrochemical water splitting. Advanced Functional Materials, 2015, 25(18): 2686–2692
46. Stolterfoht M, Le Corre V M, Feuerstein M, et al. Voltage-dependent photoluminescence and how it correlates with the fill factor and open-circuit voltage in perovskite solar cells. ACS Energy Letters, 2019, 4(12): 2887–2892
47. Akman E, Akin S, Ozturk T, et al. Europium and terbium lanthanide ions co-doping in TiO_2 photoanode to synchronously improve light-harvesting and open-circuit voltage for high-efficiency dye-sensitized solar cells. Solar Energy, 2020, 202: 227–237
48. Li Y, Zhang L, Torres-Pardo A, et al. Cobalt phosphate-modified Barium-doped tantalum nitride nanorod photoanode with 1.5% solar energy conversion efficiency. Nature Communications, 2013, 4(1): 2566
49. Yue P, She H, Zhang L, et al. Super-hydrophilic CoAl-LDH on $BiVO_4$ for enhanced photoelectrochemical water oxidation activity. Applied Catalysis B: Environmental, 2021, 286: 119875
50. Chang X, Wang T, Zhang P, et al. Enhanced surface reaction kinetics and charge separation of p–n heterojunction Co_3O_4/$BiVO_4$

Photoanodes. Journal of the American Chemical Society, 2015, 137 (26): 8356–8359

51. Li D, Liu Y, Shi W, et al. Crystallographic-orientation-dependent charge separation of $BiVO_4$ for solar water oxidation. ACS Energy Letters, 2019, 4(4): 825–831
52. Yaw C S, Ruan Q, Tang J, et al. A Type II n-n staggered orthorhombic V_2O_5/monoclinic clinobisvanite $BiVO_4$ heterojunction photoanode for photoelectrochemical water oxidation: fabrication, characterisation and experimental validation. Chemical Engineering Journal, 2019, 364: 177–185
53. Qian H, Liu Z, Guo Z, et al. Hexagonal phase/cubic phase homogeneous $ZnIn_2S_4$ n-n junction photoanode for efficient photoelectrochemical water splitting. Journal of Alloys and Compounds, 2020, 830: 154639
54. Liu Y, Wygant B R, Kawashima K, et al. Facet effect on the photoelectrochemical performance of a $WO_3/BiVO_4$ heterojunction photoanode. Applied Catalysis B: Environmental, 2019, 245: 227–239
55. Bai S, Chu H, Xiang X, et al. Fabricating of $Fe_2O_3/BiVO_4$ heterojunction based photoanode modified with NiFe-LDH nanosheets for efficient solar water splitting. Chemical Engineering Journal, 2018, 350: 148–156
56. Zhong M, Hisatomi T, Kuang Y, et al. Surface modification of CoO_x loaded $BiVO_4$ photoanodes with ultrathin p-type NiO layers for improved solar water oxidation. Journal of the American Chemical Society, 2015, 137(15): 5053–5060
57. Baek J H, Kim B J, Han G S, et al. $BiVO_4/WO_3/SnO_2$ double-heterojunction photoanode with enhanced charge separation and visible-transparency for bias-free solar water-splitting with a perovskite solar cell. ACS Applied Materials & Interfaces, 2017, 9(2): 1479–1487
58. Li S, Jiang Y, Jiang W, et al. *In-situ* generation of g-C_3N_4 on $BiVO_4$ photoanode for highly efficient photoelectrochemical water oxidation. Applied Surface Science, 2020, 523: 146441